

# Low-loss high-confinement waveguides and microring resonators in AlGaAs-on-insulator

**Ottaviano, Luisa; Pu, Minhao; Semenova, Elizaveta; Yvind, Kresten**

*Published in:*
Optics Letters

*Link to article, DOI:*
10.1364/OL.41.003996

*Publication date:*
2016

*Document Version*
Peer reviewed version

# Low-loss high-confinement waveguides and microring resonators in AlGaAs-on-insulator

**LUISA OTTAVIANO, MINHAO PU*, ELIZAVETA SEMENOVA, AND KRESTEN YVIND***

*DTU Fotonik, Department of Photonics Engineering, Technical University of Denmark, Building 343, DK-2800 Kgs. Lyngby, Denmark*
**Corresponding author: mipu@fotonik.dtu.dk, kryv@fotonik.dtu.dk*

Received XX Month XXXX; revised XX Month, XXXX; accepted XX Month XXXX; posted XX Month XXXX (Doc. ID XXXXX); published XX Month XXXX

**AlGaAs is a promising material for integrated nonlinear photonics due to its intrinsic high nonlinearity. However, the challenging fabrication of deep etched AlGaAs devices makes it difficult to realize high performance devices such as low-loss dispersion engineered waveguides and high quality microring-resonators. Here, we reported a process to make high quality AlGaAs-on-insulator wafers where high confinement waveguides can be realized. Using optimized patterning processes, we fabricated AlGaAs-on-insulator waveguides with propagation losses as low as 1 dB/cm and microring resonators with quality factors up to 350,000 at telecom wavelengths. Our demonstration opens new prospects for AlGaAs devices in integrated nonlinear photonics. © 2016 Optical Society of America**

***OCIS codes:*** *(130.0130) Integrated optics; (230.7390) Waveguides, planar; (140.4780) Optical resonators.*

http://dx.doi.org/10.1364/OL.99.099999

Integrated nonlinear photonics has recently drawn increasing research interests as it provides compact solutions compared with conventional fiber devices. Silicon-on-insulator (SOI) has been proposed as a promising platform due to its high material nonlinearity and its compatibility with the CMOS industry [1]. The enhanced device effective nonlinearity induced by the strong optical field confinement and the low linear losses ensured by the mature silicon fabrication enable various nonlinear applications such as optical signal processing [2], parametric amplification [3], supercontinuum generation [4] and frequency comb generation [5]. However, silicon suffers from two-photon absorption (TPA) when operated below 2.2 μm, which hampers its applications at e.g. telecom wavelengths (around 1.55 μm).

Aluminum gallium arsenide ($Al_xGa_{1-x}As$) is also believed to be a promising nonlinear material [6,7]. It has a large transparency window and its intrinsic material Kerr ($\chi^{(3)}$) nonlinearity (on the order of $10^{-17}$ $m^2W^{-1}$) [8-10] is larger than that of silicon. Due to its non-centrosymmetric crystal structure, AlGaAs also exhibit strong $\chi^{(2)}$ effects [11,12]. Moreover, the bandgap of the AlGaAs material can be engineered by altering the aluminum composition ($x$) to avoid TPA at telecom wavelengths. In addition, the linear refractive index of AlGaAs (around 3.3) is also similar to silicon, which makes it potentially suitable for high-index contrast waveguides. Conventional AlGaAs waveguides are realized by deep-etching a thick layer stack epitaxial grown on a GaAs substrate. The layer stack typically consists of $Al_xGa_{1-x}As$ layers with different aluminum composition ($x$) where the index of the waveguiding layer is slightly larger than that of its adjacent top and bottom layers [8-10]. The fabrication of such waveguides with very high and narrow mesa structures is challenging, and increased sidewall roughness as the etch depth is increased is typically seen which severely affects the linear loss and thus the nonlinear efficiency. Significant efforts have been taken to improve the fabrication process over past years [6-12]. Recently, Porkolab et al. demonstrated low loss deep-etched AlGaAs waveguide by using a resist reflow technique [13]. However, more advanced designs than simple waveguide such as microring resonators with integrated waveguides are still difficult to realize with high performances. For instance, the achieved quality factors ($Q$) of AlGaAs microring resonators [15-17] are much lower than those of silicon devices [5]. Therefore, most of the nonlinear processes such as second harmonic generation (SHG) [11,12] and four-wave mixing (FWM) [8-10] are demonstrated in straight AlGaAs waveguides. In addition, the low vertical index-contrast of such AlGaAs waveguides limits its effective nonlinearity in spite of high intrinsic nonlinearity.

We propose an AlGaAs-on-insulator (AlGaAsOI) platform [18,19] where a thin AlGaAs layer on top of an insulator layer resides on a semiconductor substrate allowing device patterning using an easy shallow etching process. In addition, thanks to the high index contrast in AlGaAsOI, strong light confinement waveguides can be realized to enhance device effective nonlinearities. However, compared with the conventional low-index contrast waveguides, the surface roughness control become more critical for high index contrast waveguides due to the stronger light fields at the waveguide-cladding interfaces.

In this letter, we report a newly developed wafer bonding and substrate removal process to fabricate AlGaAsOI wafers with high quality surfaces. We also optimize patterning processes such as electron-beam lithography (EBL) and dry etching to get smooth device sidewalls. We fabricated sub-micron cross-sectional dimension waveguides with a linear loss as low as 1 dB/cm. We

also fabricated microring resonators with integrated bus waveguides and obtained an intrinsic $Q$ of 350,000 for a 17-μm radius microring resonator.

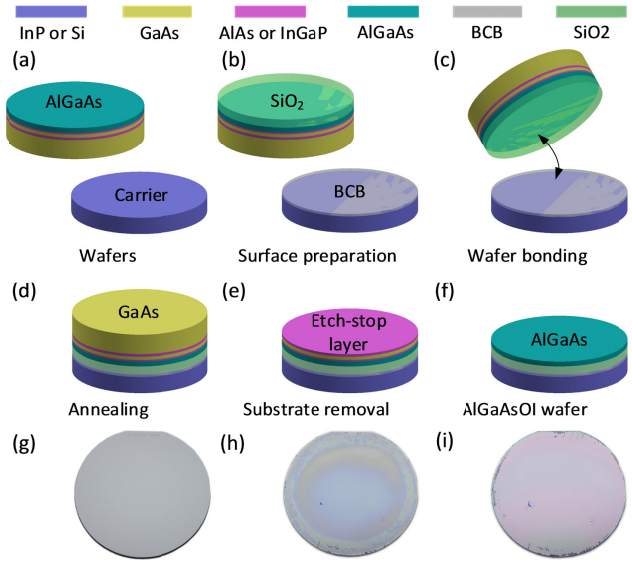


Fig. 1 Fabrication process for AlGaAs-on-insulator wafer starts with a GaAs wafer with epitaxial grown AlGaAs top layer and a semiconductor carrier wafer (a). A 3-μm $SiO_2$ layer is deposited on the AlGaAs wafer and a thin BCB layer is spun on top of the carrier wafer (b). The two wafers are then bonded (c) and annealed at 250 $^0$C (d). The thick GaAs substrate is wet-etched with the AlGaAs layer being protected by the etch-stop layer (e). After wet-etching the etch-stop layer, AlGaAsOI wafers are ready for device fabrication (f). Photos of a bonded wafer with InGaP as the etch-stop layer before (g) and after (h) the GaAs substrate is removed and after all etch-stop layer removal (i).

The fabrication process of the AlGaAsOI wafer is shown in Fig. 1. Firstly, an epitaxial stack including $Al_xGa_{1-x}As$ and etch-stop layers was grown in a low-pressure Metalorganic vapour phase epitaxy (MOVPE) reactor Emcore D125 on (100) GaAs substrates. The wafer temperature was regulated using an emissivity corrected pyrometer (RealTemp®) and the AlGaAs layer was deposited at 610°C. High quality GaAs substrates are essential in the MOVPE growth to obtain an atomic smooth surface for the AlGaAs layer. At all interfaces where group V gas was changed a 2-second growth interruption was introduced to prevent intermixing. A 3-μm thick $SiO_2$ layer is deposited by plasma enhanced chemical vapor deposition (PECVD) on the AlGaAs layer to become the buried oxide (BOX) layer. A 90 nm-thick Benzocyclobutene (BCB) layer is used as the adhesive layer for bonding between the AlGaAs wafer and another semiconductor carrier wafer (InP in this case to facilitate precise cleaving). The BCB thickness is also critical since a too thick BCB layer (e.g. >1 μm) results in difficulties in sample cleaving and inefficient thermal dissipation for the final devices while a too thin BCB layer (e.g. <50 nm) makes the wafer bonding extremely sensitive to the cleanliness of the wafer surface and thus adversely affect the yield of the wafer bonding and substrate removal processes. A thin $SiO_2$ layer and AP3000 adhesion promotor® was also deposited on the carrier wafer to enhance the BCB adhesion. The bonding process is performed under vacuum (~$3 \times 10^{-4}$ mbar) in an EVG NIL bonding machine at 250°C for 1 hour, while a force of ~750 N is applied to the bonded wafers. Subsequently, the GaAs substrate is removed in two wet etching steps including an one-hour fast etch step with a sulfuric acid/hydrogen peroxide solution ($H_2SiO_4$:$H_2O_2$=5:4) and a seven-hour slow etch step in a selective citric acid/hydrogen peroxide solution ($C_6H_8O_7$:$H_2O_2$=4:1) [20]. After the etch-stop layers (AlAs or InGaP) were wet-etched, the AlGaAsOI wafer is ready for device fabrication. Fig. 1(g-i) show photos for a bonded wafer before and after different wet etching steps. Only a few defects are observed at the edge of the AlGaAsOI wafer as shown in Fig. 1(i).

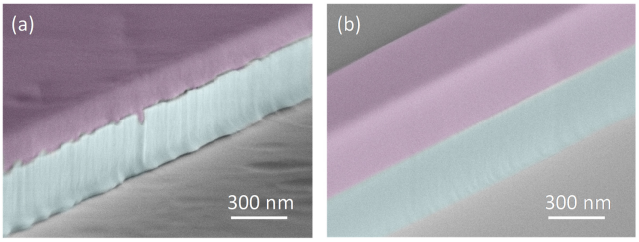


Fig. 2. Scanning electron microscopy (SEM) pictures of etched patterns on AlGaAsOI wafers fabricated by using different etch-stop layers: (a) AlAs (b) InGaP. Etch mask hydrogen silsesquioxane (HSQ) hard mask and AlGaAs material are denoted by the artificial purple and blue colour in both pictures.

A critical element in the substrate removal process is the choice of etch-stop layer as the high-index contrast device performance is very sensitive to surface roughness. We tested different etch-stop layers including AlAs and InGaP. Both AlAs and InGaP exhibit high resistance to the citric acid/hydrogen peroxide solution. Diluted hydrogen fluoride (HF) and hydrogen chloride (HCl) are used to wet-etch the AlAs and InGaP layers, respectively. Fig. 2 shows the comparison of patterns fabricated using AlGaAsOI wafers prepared using AlAs and InGaP as the etch-stop layer. It is found that the top surface of the AlGaAs layer is rough in the case of an AlAs etch-stop layer while a smooth top AlGaAs surface is observed in the case of an InGaP etch-stop layer. This large surface difference may due to byproducts in these two etching processes. In the AlAs etching process, the solid byproducts such as $AlF_3$ and $[AlF_n(H_2O)_{6-n}]^{(3-n)+}$ are hard to dissolve into the solution [21], and $As_2O_3$ can also be generated on the AlGaAs surface with a high oxygen concentration in the HF etchant [22]. Whereas, in the InGaP etching process, the etchant HCl creates highly soluble byproducts such as $AlCl_3$, $GaCl_3$, which makes it easier to obtain a smooth surface. Therefore, HCl-based wet-etching is preferred for this purpose. Alternatively InAlP can be used as the etch-stop layer with HCl being the etchant [21].

In the substrate removal process, we introduce a dual-etch-stop layer consisting of two InGaP layers with a GaAs layer in between. The etching of the thick GaAs substrate (especially in the $H_2SO_4$/$H_2O_2$ etching) is not uniform and leaves a very rough InGaP surface. As shown in atomic force microscopy (AFM) image in Fig. 3(a), a root mean square (RMS) roughness of 1.8 nm is present on the top surface after removing InGaP layer. In order to reduce the surface roughness to a sub-nanometer level as the as-grown surface, an extra GaAs/InGaP layer stack is necessary. Due to the high etching selectivity of $C_6H_8O_7$:$H_2O_2$ and HCl etchant for GaAs/InGaP and InGaP/AlGaAs layer stacks respectively, the RMS roughness of the top surface after removing the second InGaP layer is estimated to be 0.5 nm as shown in Fig. 3(b). This low roughness has insignificant influence on waveguide propagation losses compared with a typical sidewall roughness induced by dry-etching processes [23].

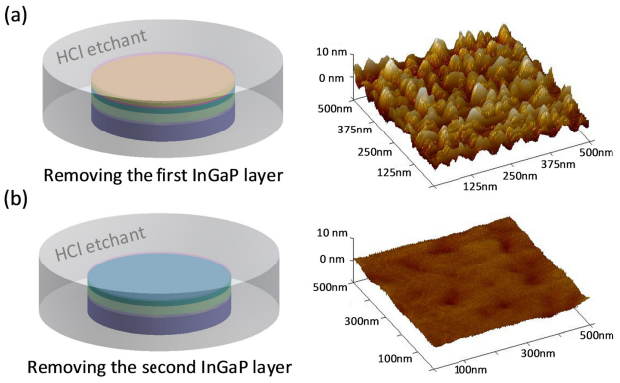


Fig. 3. Schematic illustration of wet etching of InGaP layer as the first etch-stop layer (a) and the second etch-stop layer (b) and three-dimensional atomic force microscopy (AFM) pictures for the wafer surface after the corresponding InGaP layer is removed.

For device patterning, we use hydrogen silsesquioxane (HSQ, Dow Corning FOX-15) as electron-beam resist. A 350 nm-thick HSQ layer is spun on the top of the AlGaAsOI wafer. EBL (JEOL JBX-9500FS) is used to define the patterns in HSQ with an average dosage ~10,000 μC/cm$^2$ and a KOH-based developer (AZ 400K:$H_2O$=1:3) is used for development of the HSQ. In EBL, the device pattern is fractured by the EBL software into small segments to fit the sub-field writing size (4×4 μm$^2$) determined by the sub-deflector in the EBL system. We observed small stitching between those segments after HSQ developing, which will introduce extra roughness on the sidewalls especially for bending patterns as shown in Fig. 4(a). The stitching effect may be due to resist/BOX charging [24] since an ultra-high electron beam dosage is required for the low-sensitivity HSQ. A multi-pass (exposure) EBL process can be applied to mitigate the stitching effect. In such a process, the dose for each pass is much lower than that in the single-pass EBL case, which induces less resist charging. In addition, the device pattern is also fractured differently for each pass in such a way that most of the edges of the fractured pattern segments do not overlap with those in another EBL pass. Therefore, any small stitching occurred in one pass will be smeared out by other passes. In this way, smooth curved waveguide patterning can be realized as shown in Fig. 4(b).

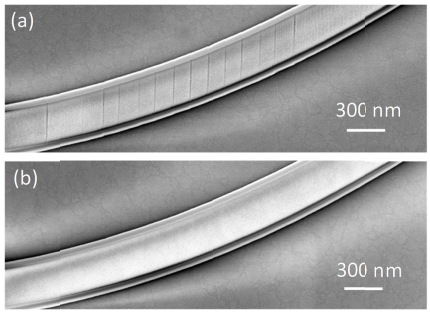


Fig. 4. EBL patterning comparison. Top-view SEM pictures of curved pattern in developed e-beam resist HSQ with different EBL processes: (a) standard single-pass EBL process, (b) multi-pass EBL process.

The device pattern was then transferred into the AlGaAs layer using a boron trichloride ($BCl_3$)-based dry etching process [25] in an inductive coupled plasma reactive ion etching (ICP-RIE) machine. To ensure a good selectivity towards the HSQ mask, straight and smooth waveguide sidewalls, critical etching parameters including chamber pressure, coil and platen power are optimized (pressure: 10 mTorr, coil/platen power: 300W/50W) for our specific SPTS ICP tool. As shown in Fig. 2(b), the fabricated sidewall surface is smooth with only small roughness at bottom of the waveguide. Finally, a 3-μm thick $SiO_2$ cladding was deposited using PECVD, and the chip was cleaved to form the input and output facets where tapers or inverse nano-tapers [26] enable efficient chip-to-fibre coupling for characterization. The masking HSQ is kept on top of the AlGaAsOI devices since the dielectric properties of HSQ is very similar to $SiO_2$, and will not adversely affect device performances [27]. In addition, HF based wet etching will also attack the $SiO_2$ under the AlGaAs devices.

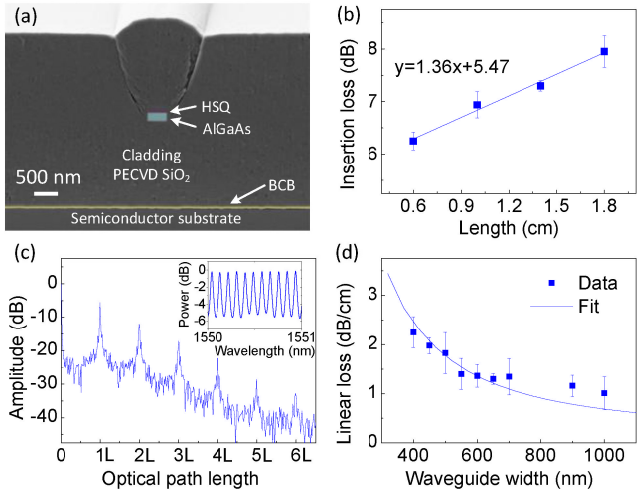


Fig. 5. (a) SEM picture showing the cross-section of an AlGaAsOI waveguide (denoted in artificial blue colour) cladded in $SiO_2$. (b) Measured insertion loss of waveguides with the same cross-sectional dimension (300 nm × 600 nm) but different lengths. (c) Fourier transform of a measured transmission spectrum (inset) for a 3-mm long waveguide (300 nm × 600 nm) with strong facet reflections. (d) The measured propagation loss of 300 nm-high AlGaAsOI waveguides with different widths (from 400 nm to 1 μm). The Payne-Lacey waveguide loss theory [28] is used for the fitting ($\sigma$=2.8 nm, $L_C$=50 nm).

To test the performance of our AlGaAsOI devices, we fabricated waveguides and microring resonators. Fig. 5(a) shows the cross-section of a fabricated AlGaAsOI nano-waveguide (300×600 nm$^2$) cladded in $SiO_2$ and Fig. 5(b) shows the measured insertion losses for the fundamental TE mode for waveguides with such a cross-sectional dimension but with different lengths. The extracted propagation loss is around 1.36 dB/cm. We also investigated the influence of waveguide width on propagation loss. Surface scattering is normally the main source for propagation loss due to roughness [28]. For high-index contrast AlGaAsOI waveguides, the propagation loss is dependent on the waveguide width since the strength of light field at the AlGaAs-$SiO_2$ interface varies resulting in a different scattering intensity as the waveguide dimension changes. Here, we utilized Fourier analysis for the loss characterization [29]. All the waveguides used for Fourier analysis are tapered to 4 μm at the chip facets to get a strong reflection and thus Fabry-Pérot fringes in the transmission spectra. The inset of Fig. 5(c) shows such a transmission for a 3-mm long waveguide (300 nm × 600 nm). The Fourier transform of the spectrum in Fig. 5(c) shows high order harmonics with constant separations (corresponds to a round-trip length $L$) and a constant harmonic amplitude ratio (HAR) (corresponds to the round-trip loss

including propagation and reflection losses) for adjacent harmonics. For the waveguides with different widths, the propagation loss difference with respect to the 600 nm-wide waveguide is then extracted by comparing the HARs for different waveguides as they all have the same chip facet reflections. As shown in Fig. 5(d), the propagation loss decreased from 2.3 dB/cm to 1 dB/cm when the width for 300 nm-thick waveguides is increased from 400 nm to 1 μm. The limit at 1 dB/cm may be attributed to top and bottom roughness or surface absorption [30].

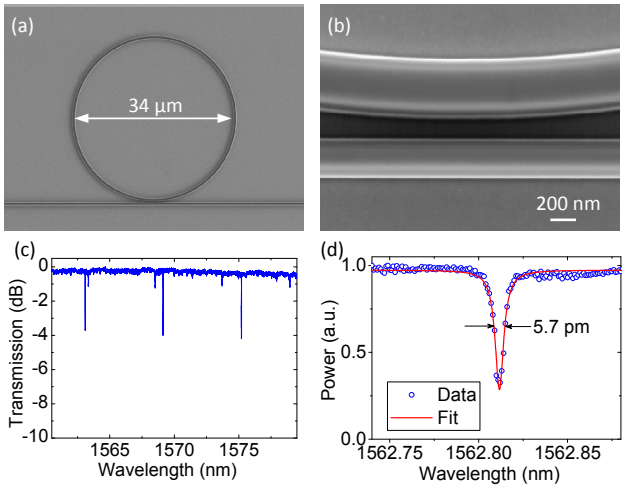


Fig. 6. (a) Top-view SEM image of the AlGaAsOI microring-resonator with an integrated bus waveguide. (b) Zoomed SEM image of the coupling region of this microring resonator. Measured (normalized) transmission spectrum of the microring resonator over a 20 nm wavelength range (c) and around the resonance at 1590 nm (d) with a loaded quality-factor ($Q$) of ~269,500.

Fig. 6(a) shows the SEM image of a fabricated 17-μm radius microring resonator. The waveguide widths for the bus and microring are 430 nm and 700 nm, respectively. The bus-to-ring coupling gap is 240 nm as shown in Fig. 6(b). Fig. 6(c) shows the transmission spectrum of this device for the TE polarization where two mode families were observed. Fig. 6(d) shows the resonance for fundamental TE mode at 1562.8 nm, which has a line-width about 5.7 pm corresponding to a loaded $Q$ of ~269,500. In the characterization, the power coupled onto chip is kept at microwatt level to avoid thermal effects. The microring resonator is operated in the under-coupling condition and the intrinsic $Q$ can be calculated by $Q_{int} = Q_{load}/(1-\sqrt{T_0})$ [31], where $T_0$ is the fraction of transmitted optical power measured at the resonance. The intrinsic $Q$ for the fundamental TE mode of our device is then estimated to be ~$3.5\times10^5$, which is the highest reported $Q$ for microring resonators fabricated using III-V materials.

In summary, we realized an integrated AlGaAsOI platform by using a newly developed process. We fabricated low-loss sub-micron waveguides and high quality factor microring resonators in this platform. The high confinement induced by the high-index contrast makes the AlGaAsOI platform very promising in various nonlinear applications such as optical signal processing [18] and frequency comb generation [19].

**Acknowledgment**. We thank Yi Zheng at Technical University of Denmark for his help on AFM measurements. Villum Fonden (Centre of Excellence: NATEC) and Teknologi og Produktion, Det Frie Forskningsråd (FTP 11-117031) funded the work.

## References

1. J. Leuthold, C. Koos, and W. Freude, *Nat. Photon.* **4**, 535 (2010).
2. L. K. Oxenløwe, H. Ji, M. Galili, M. Pu, H. C. H. Mulvad, K. Yvind, J. M. Hvam, A. T. Clausen and P. Jeppsen, *J. Sel. Top. Quantum Electron.* **18**, 996 (2012).
3. M. A. Foster, A. C. Turner, J. E. Sharping, B. S. Schmidt, M. Lipson, and L. Gaeta, *Nature* **441**, 960 (2006).
4. B. Kuyken, T. Ideguchi, S. Holzner, M. Yan, T. W. Hänsch, J. V. Campenhout, P. Verheyen, S. Coen, F. Leo, R. Baets, G. Roelkens, and N. Picqué, *Nat. Commun*. **6**, 6310 (2015).
5. A. G. Griffith, R. K. W. Lau, J. Cardenas, Y. Okawachi, A. Mohanty, R. Fain, Y. H. D. Lee, M. Yu, C. T. Phare, C. B. Poitras, A. L. Gaeta, and M. Lipson, *Nat. Commun.* **6**, 6299 (2015).
6. G. I. Stegeman, A. Villeneuve, and J. Kang, *Int. J. Nonlinear Opt. Phys.* **3**, 347 (1994).
7. J. S. Aitchison, D. C. Hutchings, J. U. Kang, G. I. Stegeman, and A. Villeneuve, *IEEE J. Quant. Electron.* **33**, 341 (1997).
8. K. Dolgaleva, W. C. Ng, L. Qian, and J. S. Aitchison, *Opt. Express* **19**, 12440 (2011).
9. C. Lacava, V. Pusino, P. Minzioni, M. Sorel, and I. Cristiani, *Opt. Express* **22**, 5291 (2014).
10. J. J. Wathen, P. Apiratikul, C. J. K. Richardson, G. A. Porkolab, G. M. Carter, and T. E. Murphy, *Opt. Lett.* **39**, 3161 (2014).
11. M. Savanier, A. Andronico, A. Lemaitre, E. Galopin, C. Manquest, I. Favero, S. Ducci, and G. Leo, *Opt. Lett.* **36**, 2955 (2011).
12. C. Ozanam, M. Savanier, L. Lanco, X. Lafosse, G. Almuneau, A. Andronico, I. Favero, S. Ducci, and G. Leo, *J. Opt. Soc. Am. B* **31**, 542 (2014).
13. M. Volatier, D. Duchesne, R. Morandotti, R. Arès and V. Aimez, *Nanotechn.* **21**, 134014 (2010).
14. G. A. Porkolab, P. Apiratikul, B. Wang, S. H. Guo, and C. J. K. Richardson, *Opt. Express* **7**, 7733 (2014).
15. D. Rafizadeh, J. P. Zhang, S. C. Hagness, A. Taflove, K. A. Stair, and S. T. Ho, *Opt. Lett.* **22**, 1244 (1997).
16. J. E. Heebner, N. N. Lepeshkin, A. Schweinsberg, G. W. Wicks, and R. W. Boyd, R. Grover, and P. T. Ho, *Opt. Lett.* **29**, 769 (2004).
17. P. Kultavewuti, V. Pusino, M. Sorel, and J. S. Aitchison, *Opt. Lett.* **40**, 3029 (2015).
18. M. Pu, H. Hu, L. Ottaviano, E. Semenova, D. Vukovic, L. K. Oxenløwe, and K. Yvind, *in Optical Fiber Communication Conference Post Deadline Papers*, OSA Technical Digest (online) (Optical Society of America, 2015), paper Th5A.3.
19. M. Pu, L. Ottaviano, E. Semenova, and K. Yvind, *arXiv:*1509.03620 (2015).
20. G. C. Desalvo, W. F. Tseng, and J. Comas, *J. Electrochem. Soc.,* **139**, 831 (1992).
21. C. Cheng, K. Shiu, N. Li, S. Han, L. Shi, and D. K. Sadana, *Nat. Commun.* **4**, 1577 (2013).
22. A. T. J. Van Niftrik, J. J. Schermer, G. J. Bauhuis, P. Mulder, P. K. Larsen, M. J. van Setten, J. J. Attema, N. C. G. Tan, and J. J. Kelly, *J. Electrochem. Soc.* **155**, D35 (2008).
23. F. Xia, L. Sekaric, and Y. Vlasov, *Nat. Photon.***1**, 65 (2007).
24. N. Kobayashi, K. Goto, T. Wakatsuki, T. Komagata, and Y. Nakagawa, *Proc. SPIE Photomask and Next-Generation Lithography Mask Technology XV*, **7028**, 70281Y (2008).
25. I. K. Beak, W. T. Lim, J. W. Lee, M. H. Jeo, G. S. Cho, and S. J. Pearton, *J. Vac. Sci. Technol. B* **21**,2487 (2003).
26. M. Pu, L. Liu, H. Ou, K. Yvind, and J. M. Hvam, *Opt. Commun.* **283**, 3678 (2010).
27. C. W. Holzwarth, T. Barwicz, and H. I. Smith, *J. Vac. Sci. Technol. B* **25**, 2658 (2007).
28. F. P. Payne and J. P. R. Lacey, *Opt. Quantum Electron.* **26**, 977 (1994).
29. D. Hofstetter, and R. L. Thornton, *Opt. Lett.* **22**, 1831 (1997).
30. D. Parrain, C. Baker, G. Wang, B. Guha, E. G. Santos, A. Lemaitre, P. Senellart, G. Leo, S. Ducci, I. Favero, *Opt. Express* **23**, 19656 (2015).
31. P. E. Barclay, K. Srinivasan, and O. Painter, *Opt. Express* **13**, 801 (2005).

## References


1. J. Leuthold, C. Koos, and W. Freude, "Nonlinear silicon photonics," *Nat. Photon*. **4**, 535–544 (2010).
2. L. K. Oxenløwe, H. Ji, M. Galili, M. Pu, H. C. H. Mulvad, K. Yvind, J. M. Hvam, A. T. Clausen and P. Jeppsen, "Silicon Photonics for Signal Processing of Tbit/s serial data signals," *J. Sel. Top. Quantum Electron.* **18** 996-1005 (2012).
3. M. A. Foster, A. C. Turner, J. E. Sharping, B. S. Schmidt, M. Lipson, and L. Gaeta, "Broad-band optical parametric gain on a silicon photonic chip," Nature **441** 960-963 (2006).
4. B. Kuyken, T. Ideguchi, S. Holzner, M. Yan, T. W. Hänsch, J. V. Campenhout, P. Verheyen, S. Coen, F. Leo, R. Baets, G. Roelkens, and N. Picqué, "An octave-spanning mid-infrared frequency comb generated in a silicon nanophotonic wire waveguide," *Nat. Commun.* **6** 6310 (2015).
5. A. G. Griffith, R. K. W. Lau, J. Cardenas, Y. Okawachi, A. Mohanty, R. Fain, Y. H. D. Lee, M. Yu, C. T. Phare, C. B. Poitras, A. L. Gaeta, and M. Lipson, "Silicon-chip mid-infrared frequency comb generation," *Nat. Commun.* **6** 6299 (2015).
6. G. I. Stegeman, A. Villeneuve, and J. Kang, "AlGaAs below half bandgap: the silicon of nonlinear optical materials," *Int. J. Nonlinear Opt. Phys.* **3** 347-371 (1994).
7. J. S. Aitchison, D. C. Hutchings, J. U. Kang, G. I. Stegeman, and A. Villeneuve, "The nonlinear optical properties of AlGaAs at the half band gap," *IEEE J. Quant. Electron.* **33** 341-348 (1997).
8. K. Dolgaleva, W. C. Ng, L. Qian, and J. I. Aitchison, "Compact highly-nonlinear AlGaAs waveguides for efficient wavelength conversion," *Opt. Express* **19** 12440-12455 (2011).
9. C. Lacava, V. Pusino, P. Minzioni, M. Sorel, and I. Cristiani, "Nonlinear properties of AlGaAs waveguides in continuous wave operation regime," *Opt. Express* **22** 5291-5298 (2014).
10. J. J. Wathen, P. Apiratikul, C. J. K. Richardson, G. A. Porkolab, G. M. Carter, and T. E. Murphy, "Efficient continuous-wave four-wave mixing in bandgap-engineered AlGaAs waveguides," *Opt. Lett.* **39** 3161-3164 (2014).
11. M. Savanier, A. Andronico, A. Lemaitre, E. Galopin, C. Manquest, I. Favero, S. Ducci, and G. Leo, "Large second-harmonic generation at 1.55 μm in oxidized AlGaAs waveguides," *Opt. Lett.* **36** 2955-2957 (2011).
12. C. Ozanam, M. Savanier, L. Lanco, X. Lafosse, G. Almuneau, A. Andronico, I. Favero, S. Ducci, and G. Leo, "Toward an AlGaAs/$AlO_x$ near-infrared integrated optical parametric oscillator,". *Opt. Soc. Am. B* **31** 542-550 (2014).
13. M. Volatier, D. Duchesne, R. Morandotti, R. Arès and V. Aimez, "Exteremly high aspect ratio GaAs and GaAs/AlGaAs nanowaveguides fabricated using chlorine ICP etchinig with $N_2$-promoted passivation," *Nanotechn.* **21** 134014 (2010).
14. G. A. Porkolab, P. Apiratikul, B. Wang, S. H. Guo, and C. J. K. Richardson, "Low propagation loss AlGaAs waveguides fabricated with plasma-assisted photoresist reflow," *Opt. Express* **7** 7733-7743 (2014).
15. D. Rafizadeh, J. P. Zhang, S. C. Hagness, A. Taflove, K. A. Stair, and S. T. Ho, "Waveguide-coupled AlGaAs/GaAs microcavity ring and disk resonators with high finesse and 21.6-nm free spectral range," *Opt. Lett.* **22** 1244-1246 (1997).
16. J. E. Heebner, N. N. Lepeshkin, A. Schweinsberg, G. W. Wicks, and R. W. Boyd, R. Grover, and P. T. Ho, "Enhanced linear and nonlinear optical phase response of AlGaAs microring resonators," *Opt. Lett.* **29** 769-771 (2004).
17. P. Kultavewuti, V. Pusino, M. Sorel, and J. S. Aitchison, "Low-power continuous-wave four-wave mixing wavelength conversion in AlGaAs-nanowaveguide microresonators,"*Opt. Lett.* **40** 3029-3032 (2015).
18. M. Pu, H. Hu, L. Ottaviano, E. Semenova, D. Vukovic, L. K. Oxenløwe, and K. Yvind, "AlGaAs-on-insulator nanowire with 750 nm FWM bandwidth, -9 dB CW conversion efficiency, and ultrafast operation enabling record Tbaud wavelength conversion," in Optical Fiber Communication Conference Post Deadline Papers, OSA Technical Digest (online) (Optical Society of America, 2015), paper Th5A.3.
19. M. Pu, L. Ottaviano, E. Semenova, and K. Yvind, "AlGaAs-on-insulator nonlinear photonics," *arXiv:*1509.03620 [physics.optics] (2015).
20. G. C. Desalvo, W. F. Tseng, and J. Comas, "Etch Rates and Selectivities of Citric Acid/Hydrogen Peroxide on GaAs, $Al_{0.3}Ga_{0.7}As$, $In_{0.2}Ga_{0.8}As$, $In_{0.53}Ga_{0.47}As$, $In_{0.52}Al_{0.48}As$, and InP," *J. Electrochem. Soc.,* **139** 831-835 (1992).
21. C. Cheng, K. Shiu, N. Li, S. Han, L. Shi, and D. K. Sadana, "Epitaxial lift-off process for gallium arsenide substrate reuse and flexible electronics," *Nat. Commun.* **4** 1577 (2013).
22. A. T. J. Van Niftrik, J. J. Schermer, G. J. Bauhuis, P. Mulder, P. K. Larsen, M. J. van Setten, J. J. Attema, N. C. G. Tan, and J. J. Kelly, "HF Species and Dissolved Oxygen on the Epitaxial Lift-Off Process of GaAs Using AlAsP Release Layers "*J. Electrochem. Soc.* **155** D35-D39 (2008).
23. F. Xia, L. Sekaric, and Y. Vlasov, "Ultracompact optical buffers on a silicon chip," *Nature* **1** 65-71 (2007).
24. N. Kobayashi, K. Goto, T. Wakatsuki, T. Komagata, and Y. Nakagawa, "Improvement of position accuracy in mask-writing electron beam lithography with a multi-pass writing strategy for reducing position errors due to resist charging," *Proc. SPIE Photomask and Next-Generation Lithography Mask Technology XV*, **7028** 70281Y (2008).
25. I. K. Beak, W. T. Lim, J. W. Lee, M. H. Jeo, G. S. Cho, and S. J. Pearton, "Comparison of dry etching of AlGaAs and InGaP in a planar inductively coupled $BCl_3$ plasma" *J. Vac. Sci. Technol. B* **21** 2487-2491 (2003).
26. M. Pu, L. Liu, H. Ou, K. Yvind, and J. M. Hvam, "Ultra-low-loss inverted taper coupler for silicon-on-insulator ridge waveguide,"*Opt. Commun.* **283** 3678-3682 (2010).
27. C. W. Holzwarth, T. Barwicz, and H. I. Smith, "Optimization of hydrogen silsesquioxane for photonic applications," *J. Vac. Sci. Technol. B* **25** 2658-2661 (2007).
28. F. P. Payne and J. P. R. Lacey, "A theoretical analysis of scattering loss from planar optical waveguides," *Opt. Quantum Electron.* **26** 977–986 (1994).
29. D. Hofstetter, and R. L. Thornton, "Theory of loss measurements of Fabry-Perot resonators by Fourier analysis of the transmission spectra," *Opt. Lett.* **22** 1831-1833 (1997).
30. P. E. Barclay, K. Srinivasan, and O. Painter, "Nonlinear response of silicon photonic crystal microresonators excited via an integrated waveguide and fiber taper," *Opt. Express* **13** 801-820 (2005).
31. D. Parrain, C. Baker, G. Wang, B. Guha, E. G. Santos, A. Lemaitre, P. Senellart, G. Leo, S. Ducci, I. Favero, "Origin of optical losses in gallium arsenide disk whispering gallery resonators," *Opt. Express* **23** 19656-19672 (2015)